Lab on a Chip

Wettability patterning for high-rate, pumpless fluid transport on open, non-planar, microfluidic platforms

Journal:	*Lab on a Chip*
Manuscript ID:	LC-ART-12-2013-051406.R1
Article Type:	Paper
Date Submitted by the Author:	29-Jan-2014

Complete List of Authors:	Ghosh, Aritra; University of Illinois at Chicago, Mechanical and Industrial Engineering Ganguly, Ranjan; Jadavpur University, Power Engineering Schutzius, Thomas; ETH Zürich, Mechanical and Process Engineering Megaridis, Constantine; University of Illinois at Chicago, Mechanical and Industrial Engineering

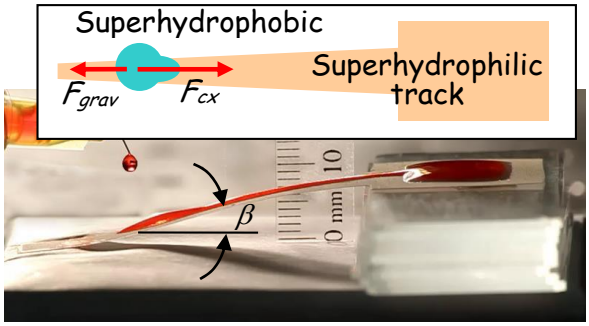

Wettability-patterned open-surface microfluidic devices facilitate pump-less transport of liquids (> 350 μLs^{-1}) and allow complex handling tasks including rise against gravity.

Wettability patterning for high-rate, pumpless fluid transport on open, non-planar microfluidic platforms†

Aritra Ghosh,[a] Ranjan Ganguly,[a,b] Thomas M. Schutzius,[a,c] Constantine M. Megaridis[a*]

[a] *Department of Mechanical and Industrial Engineering, University of Illinois at Chicago, Chicago, IL 60607, USA*

[b] *Department of Power Engineering, Jadavpur University, Kolkata 700098, India*

[c] *Department of Mechanical and Process Engineering, ETH Zürich, 8092 Zürich, Switzerland*

Abstract

Surface tension driven transport of liquids on open substrates offers an enabling tool for open micro total analysis systems that are fast becoming popular for low-cost biomedical diagnostic devices. The present study uses a facile wettability patterning method to produce open microfluidic tracks that – due to their shape, surface texture and chemistry – are capable of transporting a wide range of liquid volumes (~1 –500 μL) on chip, overcoming viscous and other opposing forces (e.g., gravity) at the pertinent length scales. Small volumes are handled as individual droplets, while larger volumes require repeated droplet transport. The concept is developed and demonstrated with coatings based on TiO_2 filler particles, which, when present in adequate (~80 wt.%) quantities within a hydrophobic fluoroacrylic polymer matrix, form

† Electronic Supplementary Information (ESI) available: Surface characterization; capillary force and acceleration of droplets; liquid capacity on wedge track; effects of prewetting and fluid properties; capillary bridging; droplet splitting on paper and polymer substrates. Videos are also available in the supplementary information.

* Corresponding author, E-mail: cmm@uic.edu

composites that are intrinsically superhydrophobic. Such composite coatings become superhydrophilic upon exposure to UV light (390 nm). A commercial laser printer-based photo-masking approach is used on the coating for spatially-selective wettability conversion from superhydrophobic to superhydrophilic. Carefully designed wedge-patterned surface tension confined tracks on the open-air devices move liquid on them without power input even when acting against gravity. Simple designs of wettability patterning are used on versatile substrates (e.g., metal, polymers, paper) to demonstrate complex droplet handling tasks, e.g., merging, splitting and metered dispensing, some of which occur in 3-D geometries. Fluid transport rates of up to 350 $\mu L\ s^{-1}$ are attained. Applicability of the design on metal substrates allows these devices to be used also for other microscale engineering applications, e.g., water management in fuel cells.

1. Introduction

Microfluidic systems on planar chips have gained popularity for handling miniscule volumes of liquids on the surface of *open* substrates. Open microfluidics offers a promising mode of digital microfluidics,[1] which involves manipulating individual droplets without the need for dedicated components like microchannels, pumps, valves, sorters or mixers. Handling liquid on open substrates also minimizes the contact between the fluid and the channel walls, thus eliminating the risk of air-bubble clogging, fouling by debris and nonspecific surface adsorption of reagents. Besides, handling isolated droplets on the digital microfluidic platform minimizes cross-contamination between samples. However, achieving regular microfluidic tasks (e.g., sample drawing, metering, merging and dispensing) in a controlled fashion remains a challenge when using open microfluidic systems. The salient requirements of a successful liquid transport strategy include: (1) rapid pumpless transport; (2) metering and controlling the liquid being dispensed; and (3) merging and splitting—nontrivial tasks. Discrete microfluidic liquid transport technology has been achieved by electrowetting-on-dielectric (EWOD),[2] optoelectrowetting (OEW),[3] magnetic force,[4] gravity,[5,6] thermocapillarity,[7] or acoustic vibrations.[8,9] Surface wettability has played a supportive role in most of these applications by ensuring the desired droplet mobility and controllability. However, these active technologies require continuous power supply (or a desired orientation of the substrates in case of gravity-driven transport), and elaborate *on-chip*/*off-the-chip* interfacing arrangements (e.g., electrode array, permanent magnet

assembly, sub-surface heating arrangement, etc.) — which for some applications are necessary — but they make their implementation more difficult.

Capillary-force driven transport of liquid droplets using spatial gradients of surface wettability has shown promise for pumpless liquid transport on open substrates. Liquid droplets on such surfaces experience an unbalanced force in the direction of increasing wettability, leading to fluid mobilization on the substrate.[10] Santos and Ondarçuhu[11] demonstrated free running droplets confined on hydrophilic tracks delimited by hydrophobic regions. They used droplets containing surface active hydrophobizing agents, which modified the surface wettability at the droplet's receding end as it rolled over the substrate. Chen et al.[12] studied Marangoni-flow induced self-propulsion of aniline droplets with limited control over motion, velocity and volume of liquid transport. Several groups have demonstrated passive transport of liquid droplets on substrates by spatially altering the surface wettability through chemical patterning,[13,14] physical texturing,[15,16,17] or a combination of both.[18,19] Bliznyuk et al.[20] used lithographically-created, anisotropic-pattern surfaces to generate surface tension gradients for actuating droplet motion. Their design yielded a maximum droplet speed of ~14 mm s^{-1}. Schutzius et al.[21] reported surface tension confined (STC) tracks that produced guided capillary transport of low surface tension liquids in a straight line with velocity approaching 30 mm s^{-1}. The fastest rate of pumpless droplet transport (velocities of 50 – 400 mm s^{-1}) has been reported through the use of triangularly-patterned, wettable tracks on superhydrophobic substrates, prepared through elaborate micropatterning and nanotexturing methods.[22] Although this work demonstrated the capacity of rapid on-chip liquid transport, it did not perform any complex flow handling tasks that are desired on lab-on-a-chip (LOC) applications. Recently Alheshibri et al.[23] extended this approach on aluminum/copper wettability patterned substrates. However the transport velocity obtained therein was an order of magnitude lower than that observed earlier by Khoo et al.,[22] while the maximum transport distance was limited to 30 mm (for wedge angle $\alpha = 4°$), and the design[23] was restricted to metal substrates.

Given a primary source of liquid pumping, an equally important task remains in guiding and confining the mobile droplets as desired on the open substrate. A few notable studies in this regard include the one by Xing et al.,[24] who reported guided transport of liquid on wettability-confined superhydrophilic tracks on superhydrophobic substrates using Laplace pressure differences. On-chip control of water droplets along arbitrarily curved wettability-confined

tracks[5] or microgrooves[6] has also been reported. Microfabricated designer STC patches[25] and chemically-patterned, triangular, superhydrophilic patches[26] on inclined substrates have also been used to guide water droplets. The former work[25] has also been extended recently to produce more complex droplet shapes and to achieve static[27] and dynamic[28,29] splitting of droplets. Balu et al.[30] achieved advanced droplet manipulation tasks like merging, transfer, splitting and storage, but used multiple substrates and extensive physical maneuvering.

Although the above mentioned works show the potential of harnessing wettability engineering for on-chip liquid transport, to date, such transport has required either very elaborate surface engineering (e.g., micro- and nano-fabrication),[18,27] produced relatively low transport rates (peak velocity mostly in the range of a few cm s^{-1}),[20,21,23] that were substrate limited, or achieved very simple modes of droplet movement.[22] For low-cost open (surface) microfluidic applications, particularly for paper-based[31,32] or textile-based[33] open microfluidics, a substrate-independent, yet straightforward surface preparation approach is more desirable.

The present study uses a facile, substrate-independent wettability patterning method to produce tapered, superhydrophilic, microfluidic tracks that are capable of inducing controlled on-chip movement of aqueous liquid volumes with characteristic size comparable to the capillary length $\kappa^{-1} = \sqrt{\gamma/\rho g}$ (γ denoting the liquid surface tension, ρ its density and g the acceleration due to gravity), by overcoming viscous and other opposing forces (e.g., gravity). The concept is developed and demonstrated with coatings based on TiO_2 powder, which, when present in optimum quantities within a hydrophobic polymer matrix, forms composites that are intrinsically superhydrophobic. Such composite coatings become superhydrophilic upon exposure to UV light. Thus, a masking process can facilitate spatially-selective conversion from superhydrophobic to superhydrophilic behavior, which is used herein to fabricate open-air devices that can move fluid efficiently without power input. Simple design features of wettability patterning have been used on versatile substrates (e.g., metals, polymers or paper) to demonstrate complex droplet handling tasks, some of which are in 3-D geometries. The present concept can be applied as building block for disposable microfluidic biosensors. Large liquid transport rates (~150 – 350 μL s^{-1}) and velocities (exceeding 400 mm s^{-1}) make the substrates suitable for high-throughput pumpless microfluidic devices. The designs are capable of handling small denominations of liquid volume (~ 1 μL) and repeated disposal of smaller liquid droplets can

lead to large (~ 500 μL) cumulative transport. While the lower volumes are applicable for common microfluidic tasks,[24] the upper volume range is relevant for on-chip liquid storage,[30] or some specialized microfluidic applications that require large volume samples (e.g., in the interrogation well of an ultra-wide field fluorescence imaging device for undiluted whole-blood samples,[34] which requires volumes ~ 1 mL). Applicability of the design on metal substrates, on the other hand, make the technique attractive for diverse engineering applications involving a wide range of liquid handling tasks, e.g., rapid chip cooling,[35] water management in fuel cells,[36] or condensate removal from the liquid collecting plate in phase change micro-thermal diode.[37]

2. Materials and Methods

Materials: The chemicals used comprise a fluoroacrylic copolymer dispersion (PMC) manufactured by DuPont (20 wt. % in water; Capstone® ST-100), titanium (IV) dioxide nanoparticles (anatase, < 25nm, 99.7% trace, Sigma Aldrich) and ethanol (~100% wt., Decon Labs). The following substrates were used: mirror-finish aluminum plate (multipurpose polished aluminum alloy 6061, 2 mm thick, McMaster Carr), transparency film for laser copiers (cross-linked polyethylene terephthalate (PET), PP2500, 3M), and white photocopier paper (80 g m^{-2}, Paper One). The PMC copolymer serves as the primary component of the superhydrophobic surface. The TiO_2 nanoparticles impart the required micro- and nano-scale roughness, and promote hydrophilicity through well-known mechanisms[38] and possible photocatalytic degradation of hydrophobic chemistries upon exposure to UV radiation.[39] All of the above materials were obtained off-the-shelf, and are readily available in the marketplace.

Methods: We used a facile and scalable approach to fabricate samples that juxtapose wettable and non-wettable spatial domains of various shapes and sizes. A typical example for synthesizing such wettability patterned coatings is presented. First, a dispersion—containing the hydrophobic PMC copolymer, TiO_2 nanoparticles, and ethanol—was prepared and subsequently spray deposited onto the substrates in order to generate a superhydrophobic surface. To synthesize the dispersion, a suspension of TiO_2 and ethanol was first formed. 1.5 g of TiO_2 was added to 14 g of ethanol, and was then probe sonicated (750 W, 13mm probe diameter, 40% amplitude, 20 kHz frequency, Sonics and Materials Inc., Model VCX-750) by supplying 1000 J of energy. Next, 2.5 g of PMC solution (20 wt. % in water) was added and shaken mechanically at room temperature to form a stable dispersion. The above solution was sprayed on three different types of substrates

(mirror-finish aluminum, PET films, and paper) using an airbrush (VL siphon feed, 0.73 mm spray nozzle, at 276 kPa (gage) air pressure, Paasch) to form a uniform coating. The spray-coated samples were then dried in a preheated oven at 60°C for 4 hours, ultimately forming a superhydrophobic surface suitable for wettability patterning. Superhydrophilic patterns were formed on this superhydrophobic surface through selectively exposing the coated substrate to UV radiation (Dymax™ 5000 EC, 400 W, 390 nm UV Source) through a photomask (a transparency film with printed black negative patterns using a common household laser printer) for 30 minutes (see Fig. 1). The UV light passed through the transparent (unprinted) section of the mask and struck the coated superhydrophobic substrate. The presence of TiO_2 in the composite promoted photocatalytic conversion of the exposed domains, rendering them superhydrophilic.[40] Complex pattern designs with features as fine as 200 μm were obtained using this photomasking technique.

Scanning electron microscopy (Hitachi S-3000N) was performed for visualizing the roughness features of the spray-deposited surface. Experiments were conducted by first mounting the substrate on a horizontal micro stage. A high-speed camera (Redlake Motion Pro, mounted with Navitar TV ZOOM 7000 or OPTEM ZOOM 100 lens) was used to capture the rapid events, such as liquid bridging, de-bridging and droplet volume splitting. The substrates were illuminated by a cool light source (FOSTEC, 8375). The real-time fluid transport features were recorded using a standard DSLR (Canon Rebel T1) camera mounted with a macro telephoto zoom lens (Sigma 70-300 mm). The water drops (~4.7 μL) were dispensed with a syringe pump (Cole-Palmer, 74900) through a 100 μm inner diameter needle (Nordson EFD, 32GA GP). The needle was strategically placed above the substrate such that the drops fell on the desired location at low speed, and the inertial effects remained negligible as compared to capillary force.

3. Results and Discussion

Scanning Electron Microscopy images of the coated substrate (see Fig. 1) show the presence of multiscale roughness features ranging from a few hundreds of nanometers to a few tens of microns, as produced by the TiO_2 nanoparticles. The parts of the substrate that were not exposed to the UV radiation retained their hydrophobicity. The average equilibrium contact angle values (computed from at least 10 sets of data for each type of surface) are listed in Table 1, while

sample images of sessile drops on each substrate are given in Fig. S1 (see ESI). As-received samples of aluminum, paper and PET films exhibited average sessile contact angles of 78.2±2°, 85.5±4°, and 8.5±2°, respectively. The micron and submicron features of the coated surface did not differ with the nature of substrate (e.g., Al plate, PET film or paper). Consequently, the superhydrophobic sections of the substrates exhibited contact angle values ranging from 151° to 156° at room temperature irrespective of the substrate (see Table 1). The UV-exposed superhydrophilic tracks, on the other hand, exhibited contact angles lower than 3°, the exact value of which could not be measured. For paper substrates, prolonged exposure to water on the superhydrophilic regions produced capillary imbibition through the substrate itself, thereby making CA measurements difficult.

3.1. Liquid transport along a wedge-shaped track

Different shapes of superhydrophilic patterns have been examined. As the simplest building block of such patterns, a wedge-shaped superhydrophilic track (akin to a long and narrow tapered path) with wedge angle α = 3° was initially chosen. Figure 2(a) shows time-lapsed images of liquid transport of a 4.7 μL droplet deposited at the narrow (left) end of a wedge track on a horizontal Al substrate (the photomask actually produced a trapezoidal shape; the droplet was deposited ~1 mm to the right from its narrowest edge, which was ~ 770 μm wide). The superhydrophilic track width where the droplet was deposited is approximately 820 μm, which is significantly narrower than the droplet diameter (~2 mm). Therefore, the liquid spreading in the transverse direction (i.e., towards the hydrophobic regions on either side of the track) was constricted by the wedge boundary. After the droplet came in contact with the track (t = 0 snapshot in Fig. 2), a rapidly advancing film front was observed to propagate ahead of the droplet towards the wider end of the track. This was driven by hemiwicking through the microscale roughness features on the superhydrophilic track.[41] The bulk of the fluid trailed behind the propagating front in the form of a liquid bulge with a progressive axial elongation (ESI, video SM1). As the liquid front advanced further along the wedge track, the bulge disappeared gradually and the liquid took the shape of a semi-conical rivulet. Prior studies have been performed on wetting morphologies of static liquid volumes confined laterally on narrow superhydrophilic tracks patterned on superhydrophobic background. Brinkmann and Lipowsky[42] have shown that the shape of such liquid accumulation on rectangular tracks depends on the ratio

Ω/δ^3 (where Ω denotes the liquid volume and δ the superhydrophilic track width). Below a critical value of Ω/δ^3, the liquid assumes a semi-cylindrical shape (elongated along the track and confined by the wettability contrast lines at the two sides of the tracks). This critical value depends on the equilibrium contact angles on the superhydrophobic and superhydrophilic domains ($\theta_{Sphobic}$ and $\theta_{Sphilic}$). The liquid volume in Fig. 2 was in a dynamic state, unlike in Ref. 42, where it was static. Nevertheless, similar bulge-like morphology was observed close to the point of deposition (i.e., $x \sim 0$) where $\Omega/\left[\delta(x)\right]^3 = 4.7/(0.82)^3 \approx 8.52$. The local track width $\delta(x)$ increases linearly with the distance x along the wedge-shaped track. Therefore, for a given volume of the deposited droplet, $\Omega/\left[\delta(x)\right]^3$ decreases with increasing x. For the image sequence in Fig. 2(a), the liquid bulge morphology was observed up to x = 14.5 mm (where δ = 1.55 mm), corresponding to $\Omega/\left[\delta(x)\right]^3 \approx 1.26$. This can be reckoned as the critical value for the track considered here. The subcritical morphology here is a bounded semi-conical shape, as opposed to a semi-cylindrical one on the rectangular track in Ref. 42.

The liquid along the wedge-shaped track is driven by the unbalanced capillary forces in the lengthwise direction, which push the droplet from a smaller wettable footprint (left) to a larger one (right). Over the initial length of 15 mm, the liquid bulge recorded an average velocity (measured as the displacement rate of the largest girth of the elongated liquid volume traveling along the track) of 110 mm s^{-1}. After the first droplet passed, the superhydrophilic channel became wet (presuffused). When an identical-size droplet was deposited at the narrow end of the presuffused track, both the liquid bulge and the propagating front behaved in a similar manner, but they exhibited even higher velocity (~ 300 mm s^{-1}) in the first 15 mm.

The initial advancement of the liquid film on the track is akin to hemiwicking of liquid on a textured superhydrophilic track.[41] However, the liquid bulge motion is strongly influenced by the Laplace pressure differential between its front and back. Figure 2(b) shows a close-up of the liquid bulge as it traveled from left to right along the wedge-shaped superhydrophilic track. The elongated droplet has a footprint that leads at the front end and trails at the rear side of the bulk with very small contact angles (due to near-complete wetting of the superhydrophilic track). The apparent contact angle $\theta(x)$ of the liquid bulge along the two straight edges of the footprint

(where the liquid contact line is pinned) does not follow Young's equation; rather it is governed by the local track width and the liquid volume contained per unit length at that particular location of the track.[43] Theoretically, this angle should be less than $\theta_{Sphobic}$ and greater than $\theta_{Sphilic}$, and would vary along the track length x. The net capillary force F_{cx} on the droplet may be obtained by taking the axial derivative of the total surface energy of the system, namely

$$F_{cx} = -\frac{d}{dx}\left[\gamma_{LS}A_{LS} + \gamma_{LG}A_{LG} + \gamma_{SG}A_{SG}\right], \quad (1)$$

where γ denotes the surface energy per unit interface area between the solid (S), liquid (L) and gas (G), and A is the corresponding surface area. Intuitively, the liquid has a propensity to move forward, as that leads to wetting of a larger area of the superhydrophilic track, resulting in a net lowering of the surface energy in the positive x direction. As seen in Fig 2(c), the liquid bulge experiences surface tension forces along the leading and trailing boundaries of the liquid footprint, and also along the pinned sidelines. Clearly, the leading edge has a larger length than the trailing one due to the wedge shape of the track. Also, the top view of the droplet in Fig. 2(b) indicates that $\theta > 90^{o}$ for most of the section of the liquid bulge that touches the pinned sidelines. Thus, along these axially diverging contact lines, the net component of surface force acts along the positive x direction. This propels the liquid droplet, a phenomenon not observed on a straight fixed-width hydrophilic track.[42] The local Laplace pressure at any section of the liquid bulge is $\sim \gamma_{LG} / r(x)$, where the local curvature of the liquid $r(x) \approx \delta(x)/\left[2\sin\theta(x)\right]$. Both $\theta(x)$ and $\delta(x)$ vary along the length of the track (for small wedge angles, $\delta(x)$ is proportional to the wedge angle α). Assuming a representative average contact angle θ_{avg} over the length of the bulge, the net axial Laplace pressure gradient in the liquid bulge can be estimated as

$$\frac{dP}{dx} \sim -\frac{d}{dx}\left[\frac{\gamma_{LG}}{r(x)}\right] \sim -\gamma_{LG}\frac{d}{d\delta(x)}\left[\frac{2\sin\theta(x)}{\delta(x)}\right]\frac{d\delta(x)}{dx} \sim 2\gamma_{LG}\sin\theta_{avg}\frac{1}{\delta(x)^2}\alpha. \quad (2)$$

This pressure gradient is responsible for driving the droplet to the wider portions of the wedge track. Equation (2) indicates that the capillary pressure gradient is proportional to the wedge angle α and inversely proportional to the square of local track width $\delta(x)$. However, evaluating the magnitude of the capillary force from this expression requires *a priori* knowledge of how the angle $\theta(x)$ varies with x, which requires computational analysis.[42] A separate experiment was

therefore carried out (see Fig. 3(a)) under a static scenario following the approach of Lorenceau and Quéré[44] to calculate the capillary force on the droplet at the onset of the motion. The substrate was mounted on a tilt platform with a large enough inclination so that a droplet placed at the narrow end of the presuffused wedge did not move up. The tilt angle β was gradually reduced until the capillary force became comparable to the in-plane component of the droplet weight, so that the droplet moved up the plane. For a known droplet volume Ω (the test was repeated with different volumes of dispensed droplets) and β measured from the experiment, the capillary force (at the narrow end of the wedge track) can therefore be calculated as

$$F_{cx} = \rho \Omega g \sin\beta . \qquad (3)$$

Figure 3(b) shows the variation of capillary force on the droplets with the wedge angle. Each data point represents about 100 readings taken with dispensed droplet volumes ranging from 4.7 μL to 23.5 μL (the readings of β, and hence the F_{cx} did not vary much with Ω – see Section S2 and Fig S2 in ESI for details – while the error bars represent the standard deviation in reading). Clearly, the linear nature of the plot of F_{cx} against α shows conformity to Eq. (2). The capillary force for the case shown in Fig. 2 (i.e., $\alpha = 3^o$) is found to be approximately 56.3 μN, which would, in absence of any restrictive forces produce an instantaneous acceleration of 12 m s^{-2} for a 4.7 μL droplet. The observed acceleration on a horizontal substrate could differ from this value since the actual bulge volume is slightly less than 4.7 μL (part of the liquid spread by hemiwicking). Also, in reality, the motion of the liquid bulge is resisted by contact angle hysteresis (CAH) between its advancing and receding fronts, as well as viscous forces.[22] The effects of the first two factors (loss of liquid from the bulge due to hemiwicking, and the restrictive force due to CAH) have competing influence on the droplet acceleration, while the viscous force on the droplet at the onset of its motion is negligible. Later in this section, we shall see that the predicted value of acceleration indeed matched closely with the observed initial acceleration of the liquid bulge on a presuffused track.

At the far downstream portion of the wedge track, the contact angles at the pinned sidelines may become less than 90^o, thus having a contribution that resists the forward motion of the bulk liquid (see Fig. 2(c)). This may lead to a flagging F_{cx} at the downstream portion of the tracks,[23] forcing the droplet transport to cease. However, for the geometry considered in Fig. 2, and the liquid volumes dispensed herein, sustained forward movement of the droplets persisted

until the droplets reached the wide edge of the track (travel path ~25mm). Subsequent droplets (deposited afterwards at the same location) also exhibited similar behavior on the presuffused track, although these moved faster. The track kept pumping the liquid from the narrower end and accumulating it at the wider end in the form of a growing bulge (the latter happened if the accumulated volume exceeds the threshold value discussed before). A separate study on a 60 mm long wedge-shaped track having $\alpha = 4^o$ showed that the track was able to hold 235 μL of water in a rivulet shape before bulging out at its wider end (see Fig. S3 in ESI).

Figure 4 shows (a) the displacement-time (on x-$t^{1/2}$ axes) and (b) the velocity-displacement profiles of the liquid front and the bulge on a dry track and on a presuffused track. Each plot represents readings averaged over at least six independent runs, while the error bars show the standard deviation. As seen from Fig. 4, the liquid front begins to spread along the dry track at a high speed (~165 mm s^{-1} at x= 1.9 mm) but it gradually slows down (~90 mm s^{-1} at x = 7 mm) as the liquid film spreads down the track. This propagation can be attributed to the capillary wetting of the textured philic track by the liquid. Typical capillary wetting would exhibit the Washburn profiles[21] for displacement-time and velocity-displacement plots, following $x = \sqrt{\gamma_{LG} d_{pore} t / 4\mu}$ (straight line on x-$t^{1/2}$ plot), and $V \sim \gamma_{LG} d_{pore} / \mu x$ (rectangular hyperbola on V-x plot), respectively. The hemiwicking displacement and velocities for Washburn flow are also plotted in Fig. 4 for water (γ_{LG} = 72.1 mN m^{-1}, dynamic viscosity μ = 0.89 mPa s), assuming an estimated mean surface feature size (created by the TiO_2 particles) d_{pore} = 40 μm. Although pore size was used as a fitting parameter, the optimal value is consistent with the size of aggregated TiO_2 particles that create the surface texture. The observed displacement plot for the liquid front showed agreement with the Washburn profile for approximately the first 5 mm of travel (see Fig. 4(a)), and exceeded the latter significantly in the downstream region. The liquid bulge, on the other hand, exhibits a relatively sluggish start due to its inertia, but it soon speeds up to closely follow up the liquid front. Beyond x ~ 7 mm the liquid bulge is found to move at nearly the same velocity with the front, trailing it by ~2 mm, until the bulge shape disappears. At this stage, the liquid bulge following the hemiwicking front acts as a "source" that offers the driving potential for the liquid front to propagate further ahead. This eventually causes the liquid front's velocity to exceed that predicted from the Washburn equation (Fig. 4(b)).

On a presuffused track, the effective capillary pore diameter (d_{pore}) is larger than that exhibited by the dry tracks since the finer microstructure features on the surface remain submerged, leaving only larger surface "apex" features to influence hemiwicking (see Section S4 in ESI). Thus, the initial velocity of the hemiwicking front on a presuffused track should be much larger. Indeed, as seen in Fig. 4, the liquid front on a presuffused tack recorded an initial velocity ~ 424 mm s^{-1}, which approximates a Washburn velocity profile corresponding to d_{pore} = 150 μm (optimal value obtained by fitting the experimental data). As in the case of a dry track, the liquid bulge on a presuffused track also accelerated from rest, and gradually moved faster. The acceleration of the liquid bulge at the inception of the droplet motion was found to be $\mathrm{d}V/\mathrm{d}t\big|_{t=0} = 12.3$ m s^{-2} (see Section S5 of ESI). This is in excellent agreement with the acceleration (12 m s^{-2}) evaluated from the capillary force diagram (Fig. 3(b)). Beyond x ~ 6 mm, the liquid bulge velocity exceeded the velocity of the front, but was not able to catch up within the available track length. The front velocity also picked up speed as it received better "feed" from the liquid bulge trailing right behind it. Figure 4 clearly indicates that the motion of the liquid front through the wedge-shaped superhydrophilic track follows the Washburn behavior only in the first few millimeters of the track length beyond which the advancing velocity is significantly bolstered by the liquid bulge trailing behind the propagating meniscus. Similar behavior was also observed when water droplets containing 10% ethanol (by wt.) were transported on the same wedge track, but the average velocity was lower (~83% of that observed with pure water) due to the lower surface tension (47.5 mN m^{-1}) and higher viscosity (1.21 mPa-s) of ethanol-water mixture.

3.2. Liquid transport using complex patterns

3.2.1 Droplet metering, merging and rapid transport

Having established the pumping capability of the individual wedge-shaped tracks, more complicated surface patterns comprising of these tracks were designed to demonstrate multi-step functionalities. It is apparent from the previous section that the wedge-shaped tracks transport the liquid towards the wider end either in the form of a bulge (early) or a semi-conical rivulet (late). If two such tracks are laid parallel to each other, and the Ω/δ^3 ratio for the track (δ being the track width at the wider end) is large enough to favor the "bulge morphology," it is possible to

generate two juxtaposed liquid bulges with the potential to interact with one another towards certain functionalities. For example, if the intervening space between the adjacent tracks is comparable to the lateral width of each liquid bulge, the menisci of the accumulated liquids at the wider ends of the tracks would merge to form a liquid bridge.[45] The critical volume at which the liquid bridge occurs depends on the geometrical features of the tracks and their lateral spacing. This provides a design tool for metering precisely the volume of pumped liquid that eventually forms a bridge between the two tracks. The device design we attempt, therefore, comprises of three wedge-shaped tracks; Fig. 5(a). Tracks A and B are 21.5 mm long with wedge angle of 1^o spaced parallel to each other at an axis-to-axis pitch of 3.6 mm, while track C, 21.5 mm long with wedge angle of 10^o is placed in tandem. A 1.5 mm × 0.5 mm rectangular superhydrophilic strip D protrudes from track C between tracks A and B to facilitate the liquid draining process (as described below). Water droplets were dispensed one-at-a-time using metering syringes placed over the narrow ends of tracks A and B and were transported spontaneously to their wider ends, where $\delta \sim 720$ μm. Even with the first pair of droplets (4.7 μL each) deposited, the ratio $\Omega \Big/ \left[\delta(x)\right]^3 \sim 12.6$, which is an order of magnitude higher than the critical value mentioned in Section 3.1. This is corroborated by the observation of liquid bulges formed at the ends of tracks A and B and their growth until they attain the state shown in Fig. 5(b). For the given spacing between tracks A and B on the aluminum substrate, the two bulges touched at their largest girth (see Figs. 5(b) and (b1)) after each channel received 7 droplets of 4.7 μL each (i.e., a total of 65.8 μL). Figures 5(c) and (c1) show the onset of liquid bridging caused by the merger of the two bulges. The bridge grew immediately due to coalescence of the two volumes (Figs. 5 (d, e) and (d1, e1)). The liquid bulges had oblong shape (axial extent nearly 2.5 times their lateral spread), as seen from the top in Fig. 5 (b – e); the end view of the same event is shown in Fig. 5 (b1 – e1). The bridge height as recorded in Figs. 5(b1 – e1) may be treated as the characteristic bridge dimension during coalescence. Over the first 5 ms of bridge formation, the droplet bridge height grew with the square root of time (see Fig. S6 in ESI), which is typical of a droplet coalescence scenario where capillary and inertial forces dominate.[46] The liquid bridge eventually touched the intervening superhydrophobic surface (Fig. 5(e1)) and rested on it in a Cassie (non-wetting) state,[47] as is evident from the visible glossy texture underneath it (see white arrow in Fig. 5(e)). The curvature of the liquid bridge is seen to create a

"lens" effect so that micro-scale surface texture details of the superhydrophobic region become magnified, and thus more visible. The liquid bridge kept expanding axially due to the inertial effect at the expense of the lateral spread of the bulge when ultimately it touched the narrow end of strip D (see frame 5(g)). The liquid then hemiwicked through the superhydrophilic strip and advanced onto track C when the final stage of pumping began (frame 5(h)). The liquid in the bridge was pumped through track C from t = 24 ms through t = 208.5 ms (see frames 5(h) through 5(l)) until the pool drained completely and de-bridged from tracks A and B. With continual dispensing of droplets at the loading (narrow) end of tracks A and B, the cycle of bridging, spreading, pumping and de-bridging can be repeated as many times as needed (see ESI, video SM2 for one complete cycle). Between the events of the liquid bridge touching track D (Fig. 5 (g)) and the de-bridging (Fig. 5 (l)), the device pumped at an average rate of 357 μL s^{-1} without any external power input. More importantly, the quantity of transposed volume, which can be controlled by altering the geometry of the tracks, is highly repeatable.

The design performed equally well on PET film and paper, as it did on metal. Figure 6(a) shows the different stages of a similar cycle of bridging, pumping and de-bridging on a horizontal paper substrate (the water was dyed red for better visualization). For the same dimensions of track patterns as in Fig. 5 (Al substrate), the bridging of liquid accumulated on tracks A and B in Fig. 6(a) occurred once after each track received 6 droplets (each measuring 4.7 μL), thus pumping approximately 56.4 μL per cycle. Similar pumping behavior was also observed on PET film. Figure 6(b) shows snapshots of liquid accumulation on a PET film substrate on track C after the device has pumped for 1, 4, 7 and 10 continuous cycles. Figures 6(b3) and (b4) show that the drained liquid rests on track C showing a bulge morphology, with the liquid pinned on the wettability contrast line along the periphery of the larger track. The maximum storage capacity of track C is, limited by the track area and the value of $\theta_{Sphobic}$. If the liquid is suitably drained out from the downstream end of track C (e.g., by providing a larger superhydrophilic well or by capillary wicking), the device will pump repeatedly for an indefinite period. On both aluminum and PET film substrates, the design was found to exhibit continual pumping at the same cycle volume until track C is filled up to a level that the contact line could no longer be pinned at the borders of the track. For a paper substrate, the repeatability was compromised by selective imbibition in the substrate itself through the philic track due to prolonged exposure to water. Therefore, for paper based substrates, long-term performance is not

warranted. However, the paper-based substrate may be used as an ideal choice for inexpensive single-use microfluidic devices.

3.2.2 Droplet splitting in multiple equal volumes

Droplet splitting is an important task in digital microfluidics, as for example when a given sample volume needs to be split for feeding a multiplexed microfluidic architecture. Figure 7 (a) shows the design of a droplet splitter that has 3 identical wedge-shaped superhydrophilic tracks (23mm in length, wedge angle 4^o), each laid radially outward from a common center at 120^o angular spacing. The narrow ends of the wedge-shaped tracks are spaced 800 μm from the center, which is marked by a 400 μm circular hydrophilic spot to allow droplet anchoring during deposition on the substrate. Figures 6(b1) – (b6) show the time-lapsed images of an event after a 4.7 μL droplet was deposited on the central philic spot. As the droplet was dispensed on the substrate (Fig. 7(b1)), the outer rim of its base touched the narrow ends of the radial tracks (Fig. 7(b2)) upon impact; the liquid quickly spread along the superhydrophilic radial tracks, forming a liquid bridge that connected the three tracks and the central philic spot (Fig. 7(b3)). The pumping continued from the central spot with a liquid front propagating along each track (Fig. 7(b4, b5)) till the central liquid volume de-bridged at the inner ends of the track (Fig. 7(b6)), leaving a very small residual droplet at the central philic spot. The salient advantage of this design from the one proposed by Lee et al.[28] is that the residual central volume is much smaller than the original droplet volume, with no liquid bridging the split radial volumes. Thus, for an LOC application this design eliminates the possibility of cross-contamination. As observed from the timestamps in Fig. 7(b), the droplet took 30 ms to fragment between the central spot and the three radial tracks – corresponding to a pumping rate of ~157 μL s^{-1}. For a uniform split, each track in Fig. 7 transported ~ 1.5 μL volume. The splitter design was also successfully tested on paper and PET film (see Fig. S7 in ESI). It is important to note that irrespectively of the substrate, the uniformity of volumes collected at the end of each track is found to be very sensitive to the precision with which the original droplet is deposited on the central spot. Any eccentricity or bias in the position of the liquid dispenser leads to unequal liquid distribution (see Fig. S7b in ESI). This feature can therefore be used as a tool for two-dimensional microfluidic position sensing. Splitter designs with higher number of radial arms (with same track size and distance of inner ends from

central philic spot) are also demonstrated in Fig. S7c in ESI and video SM3 where each splitter arm is shown to transport ~ 1μL liquid per cycle.

3.2.3 Liquid transport up an incline

Use of flexible substrates like paper and transparency (PET) films allows the ability to attain out-of-plane liquid transport. In order to realize such transport, the capillary force has to overcome gravity in part of the microfluidic circuit. The wedge-shaped superhydrophilic tracks on a superhydrophobic paper or PET film surface have already been found capable of producing rapid liquid transport on horizontal substrates. Figure 8 shows that the capillary force produced on the droplet by the wedge-shaped track is also strong enough to move the liquid up along an inclined substrate. Figure 8(a1-a3) shows images of liquid being pumped up a ramp to an elevation of 9 mm (see ESI, video SM4). This corresponds to an approximate ramp tilt angle of 13° for the flexible PET film substrate, although the ramp appears slightly curved due to the flexibility of the PET film. Figures 8(a2 and a3) show a residual volume of liquid left behind on the inclined superhydrophilic track after pumping a given volume to the reservoir on the top. After transporting a total of 50 drops (235 μL) of water up the ramp, the track was found to retain only 14 μL, a small portion of the total volume propelled to the top. Similar pumping was also observed on paper where the same design was found to transport 117.5 μL of water up a height of 4 mm along a ramp angle of ~8^o; see Fig. 8(b). Figure 8(c) depicts the template design used for the PET and paper substrates.

Pumping of liquid against gravity by the wedge-shaped superhydrophilic pattern works well also for the liquid bridging/draining circuit (Figs. 5, 6). A PET substrate was used to create a three-dimensional platform where the substrate had two horizontal parts at two different elevations, connected by an inclined section. Figure 9 shows select snapshots as a liquid bridge formed between two parallel wedge-shaped tracks A and B on the horizontal part (I) of the substrate, and then the bridged liquid was pumped along the third track C (II), laid on the inclined part of the substrate at 13° tilt up to a height of 4 mm. The bridging, draining and de-bridging modes of liquid transport on the non-planar substrate were similar to those observed on a horizontal surface (Figs. 5 and 6), with the only difference that the pumping rate for the inclined substrate was ~ 156 μL s^{-1} as opposed to 357 μL s^{-1} on the horizontal plane. All the cases presented in Figs. 8 and 9 showed pumpless transport, where the spatial difference of

surface energy on the substrate is utilized to overcome the viscous resistance and gravity force. In principle, the technique works with a combination of up and down ramps, thus offering limitless possibilities for the construction of 3-D microfluidic arrangements that are capable of transporting liquid at considerable rates. The present examples demonstrate the prospect of complicated microfluidic networks (e.g., open channels in the form of crossovers) on microfluidic platforms for enhanced device functionality.

4. Conclusions

We have developed a facile, substrate-independent, wettability patterning method and demonstrated controlled transport of liquid at large volume flow rates (~350 μL s^{-1}) on flat and inclined substrates. Wedge-shaped superhydrophilic planar tracks laid on superhydrophobic background have been used as the building blocks of the designs. Liquid dispensed at the narrow ends of a superhydrophilic wedge track gets transported to the wider ends by hemiwicking and Laplace pressure-driven flows. The driving capillary force increases linearly with the wedge-angle of the tracks. However, the travel distance diminishes with wedge angle. Thus, balancing rapid transport rate and distance presents an optimization problem. The motion of liquid on the wedge track, in the form of a wetting front followed by an advancing liquid bulge, has been found to surpass the classical Washburn type, yielding velocities exceeding 400 mm s^{-1}. Liquid transport speed increases on prewetted tracks. More complex manipulations involving liquid metering, merging and dispensing have been achieved by patterning two closely-spaced parallel wedge tracks in tandem with another similar track of larger wedge angle. A juxtaposed pair of liquid bulges accumulated at the ends of two parallel dispensing tracks coalesced once a specific volume of liquid was accumulated, and the merged droplet was transported downstream through the third track spontaneously by capillary action, eventually detaching the liquid from the original dispensing tracks. The events of droplet bridging, pumping and de-bridging are highly periodic and precise in terms of the dispensed droplet volumes. The design is capable of pumping liquid volumes ranging from 1 μL (5-split design) to over 500 μL (through repeated disposal of smaller liquid droplets, avoiding any back-flow). Both the single-wedge and the droplet-bridging designs demonstrated additional capability of moving liquid up along inclined substrates without any external power input, thus providing means of transport in 3-D microfluidic systems. A radially outward array of wedge tracks has also been designed to create

a droplet splitting arrangement. Droplets carefully deposited on a central philic spot were quickly and equally split amongst the tracks that transported the liquid outward with minimal cross-contamination between the split volumes. For a three-split design, a pumping rate of ~150 μL s^{-1} was recorded. The surface functionalization methods and track designs have been found to work equally well on metal, paper and polymer film substrates. The concept can be implemented for pumpless liquid transport in a variety of engineering applications ranging from paper-based microfluidic devices to 3-D microfluidics, or for condensate management in fuel cells.

Acknowledgements

The authors acknowledge the financial support of the U.S. National Science Foundation (STTR Grant 1331817 via NBD Nano), and NBD Nano. We thank Zachariah Rabatah (UIC) and Jared Morrissette (UIC) who performed preliminary experiments that led to the selection of the coating composition.

References

1 K. Choi, A. H. C. Ng, R. Fobel and A.R. Wheeler, *Ann. Rev. Anal. Chem.*, 2012, **5**, 413–440.

2 W. C. Nelson and C. -J. Kim, *J. Adhesion Sci. Tech.*, 2012, **26**, 1747–1771.

3 S. -Y. Park, M. A. Teitell and E. P. Y. Chiou, *Lab Chip*, 2010, **10**, 1655–1661.

4 Z. Long, A. M. Shetty, M. J. Solomon and R. G. Larson, *Lab Chip*, 2009, **9**, 1567–1575.

5 J. Seo, S. Lee, J. Lee and T. Lee, *ACS Appl. Mater. Interface*, 2011, **3**, 4722–4729.

6 H. Mertaniemi, V. Jokinen, L. Sainiemi, S. Franssila, A. Marmur, O. Ikkala and R.H.A. Ras, *Adv. Mater.*, 2011, **23**, 2911–2914.

7 A. A. Darhuber, J. P. Valentino, S. M. Troian and S. Wagner, *J. Microelectromech. Syst.*, 2003, **12**, 873–879.

8 Z. Wang and J. Zhe, *Lab Chip*, 2011, **11**, 1280–1285.

9 D. Foresti, M. Nabavi, M. Klingauf, A. Ferrari and D. Poulikakos, Proc. Nat. Academey Sci., 2013, 110, 12494–12554.

10 A. A. Darhuber and S. M. Troian, *Ann. Rev. Fluid Mech.*, 2005, **37**, 425–455.

11 F. D. D. Santos and T. Ondarçuhu, *Phys. Rev. Lett.*, 1995, **75**, 2972–2974.

12 Y. -J. Chen, Y. Nagamine and K. Yoshikawa, *Physical Rev. E*, 2009, **80**, 016303.

13 M. K. Choudhury and G.M. Whitesides, *Science*, 1992, **256**, 1539–1541.

14 E.S. Kooji, H.P. Jansen, O. Bliznyuk, B. Poelsema and H.J.W. Zandvliet, *Colloids Surfaces A: Physicochem. Eng. Aspect*, 2012, **413**, 328–333.

15 C. Lv and P. Hao, *Langmuir*, 2012, **28**, 16958–16965.

16 J. -T. Yang, Z. -H. Yang, C. –Y. Chen and D-J Yao, *Langmuir*, 2008, **24**, 9889–9897.

17 A. D. Sommers, T. J. Brest and K. F. Eid, *Langmuir*, 2013, **29**, 12043−12050.

18 B. Chandesris, U. Soupremanien and N. Dunoyer, *Colloids Surfaces A: Physicochem. Eng. Aspect*, 2013, **434**, 126–135.

19 Y. -H. Lai, J. -T. Yang and D. –B. Shieh, *Lab Chip*, 2010, **10**, 499–504.

20 O. Bliznyuk, H. P. Jansen, E. S. Kooij, H. J. W. Zandvliet and B. Poelsema, *Langmuir*, 2011, **27**, 11238–11245.

21 T. M. Schutzius, M. Elsharkawy, M. K. Tiwari and C. M. Megaridis, *Lab Chip*, 2012, **12**, 5237–5242.

22 H. S. Khoo and F. -G. Tseng, *Appl. Phys. Lett.,* 2009, **95**, 063108.

23 M. H. Alheshibri, N. G. Rogers, A. D. Sommers and K. F. Eid, *Appl. Physics Lett.*, 2013, **102**, 174103.

24 S. Xing, R.S. Harake and T. Pan, *Lab Chip*, 2011, **20**, 3642–3648.

25 V. Jokinen, L. Sainiemi, and S. Franssila, *Adv. Mater.*, 2008, **20**, 3453–3456.

26 A. Nakajima, Y. Nakagawa, T. Furuta, M. Sakai, T. Isobe and S. Matsuhita, *Langmuir*, 2013, **29**, 9269–9275.

27 V. Jokinen, R. Kostiainen and T. Sikanen, *Adv. Mater.*, 2012, **24**, 6240–6243.

28 M. Lee, Y. S. Chang, H. –Y. Kim, *Phys. Fluids*, 2010, **22**, 072101.

29 S. Kim, M-W. Moon, H.-Y. Kim, *J. Fluid Mech.*, 2013, **730**, 328–342.

30 B. Balu, A. D. Berry, D. W. Hess and V. Breedveld, *Lab Chip*, 2009, **9**, 3066–3075.

31 G. Chitnis, Z. Ding, C. -L. Chang, C. A. Savran and B. Ziaie, *Lab Chip*, 2011, **11**, 1161–1165.

32 A. W. Martinez, S. T. Phillips, M. J. Butte and G. M. Whitesides. *Angew. Chem., Int. Ed.*, 2007, **46**, 1318–1320.

33 S. Xing, J. Jiang and T. Pan, *Lab Chip*, 2013, **13**, 1937–1947.

34 Z. Göröcs, Y. Ling, M. D. Yu, D. Karahalios, K. Mogharabi, K. Lu, Q. Wei and A. Ozcan, *Lab Chip*, 2013, **13**, 4460–4466.

35 J. –T. Cheng and C. –L. Chen, *Nanoscale Microscale Thermophysical Eng.*, 2010, **14**, 63–74.

36 S. G. Kandlikar, *Heat Transfer Eng*., 2008, **29**, 575–587.

37 T. Hirayanagi, T. Tsukamoto, M. Esashi, and S. Tanaka, *Journal of Physics: Conference Series*, 2013, **476**, 012019.

38 M. Takeuchi, K. Sakamoto, G. Martra, S. Coluccia, M. Anpo, *J. Phys. Chem. B*, 2005, **109**, 15422

39 M. Yang, Z. Di, J. -K. Lee, *J. Colloids Interface Sci.*, 2013, **368**, 603 - 607.

40 K. Tadanaga, J. Morinaga, A. Matsuda and T. Minami, *Chem. Mater.*, 2000, **12**, 590–592.

41 D. Quéré, *Annu. Rev. Mater. Res*., 2008, **38**, 71–99.

42 M. Brinkmann and R. Lipowsky, *J. Appl. Phys.*, 2002, **92**, 4296–4306.

43 H. Gau, S. Herminghaus, P. Lenz and R. Lipowsky, *Science*, 1999, **283**, 46–49.

44 É. Lorenceau and D. Quéré, *J. Fluid Mech.*, 2004, **510**, 29–45.

45 H. Kusumaatmaja and R. Lipowsky, *Langmuir*, 2010, **26**, 18734–18741.

46 R. T. Eiswirth, H. -J. Bart, A. A. Ganguli, and E. Y. Kenig, *Physics Fluids*, 2012, **24**, 062108.

47 A. B. D. Cassie, S. Baxter, *Trans. Faraday Society* 1944, **40**, 546–551.

Table 1: Sessile contact angle (θ_e)* values on various substrates

	Uncoated Substrate	Coated Substrate (Hydrophobic part)	Coated Substrates (Hydrophilic part)
Aluminum	78.2 ±2^o	151.2 ±2.3^o	**
Paper	85.5 ±4^o	154.5 ±2^o	**
PET film	8.5 ±2^o	156 ±3^o	**

* Contact angle data evaluated from sets of at least 10 readings.

** Contact angles too low to measure

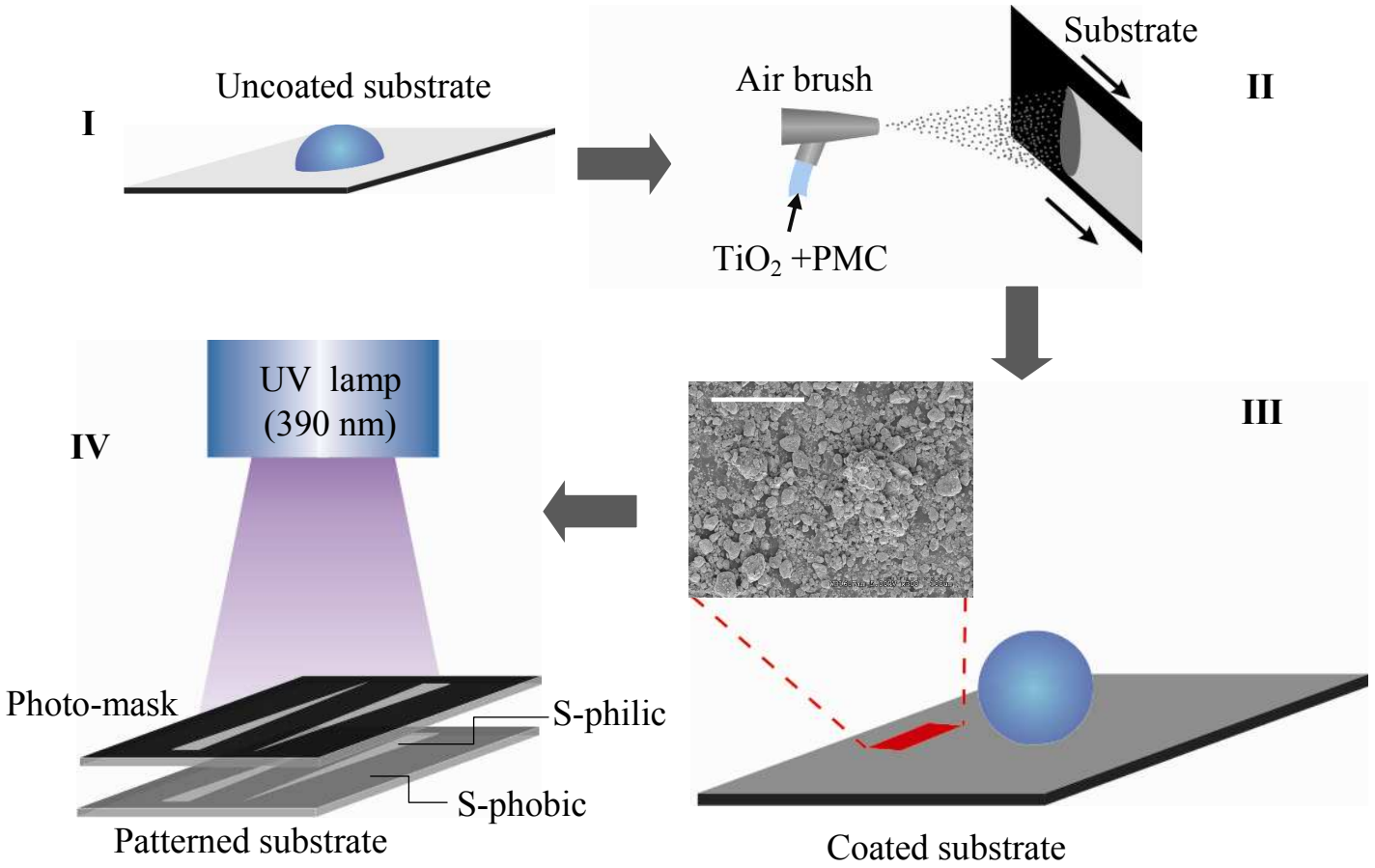

Figure 1: Salient steps of surface preparation. (I) Uncoated substrate (Aluminum, PET film or regular white paper). (II) Spray-coating of TiO_2-PMC aqueous suspension on substrate. (III) Coated substrate, and SEM image of the coated surface showing the different length scales of the deposited nanoparticle composite coating. Combination of PMC and the roughness imparted by the TiO_2 particles renders the surface superhydrophobic (water beads). (IV) UV treatment of the superhydrophobic substrate through a patterned photomask to form the superhydrophilic regions. Exposed regions turn superhydrophilic (S-philic) upon 30 minutes of exposure to UV, while the unexposed regions remain superhydrophobic (S-phobic).

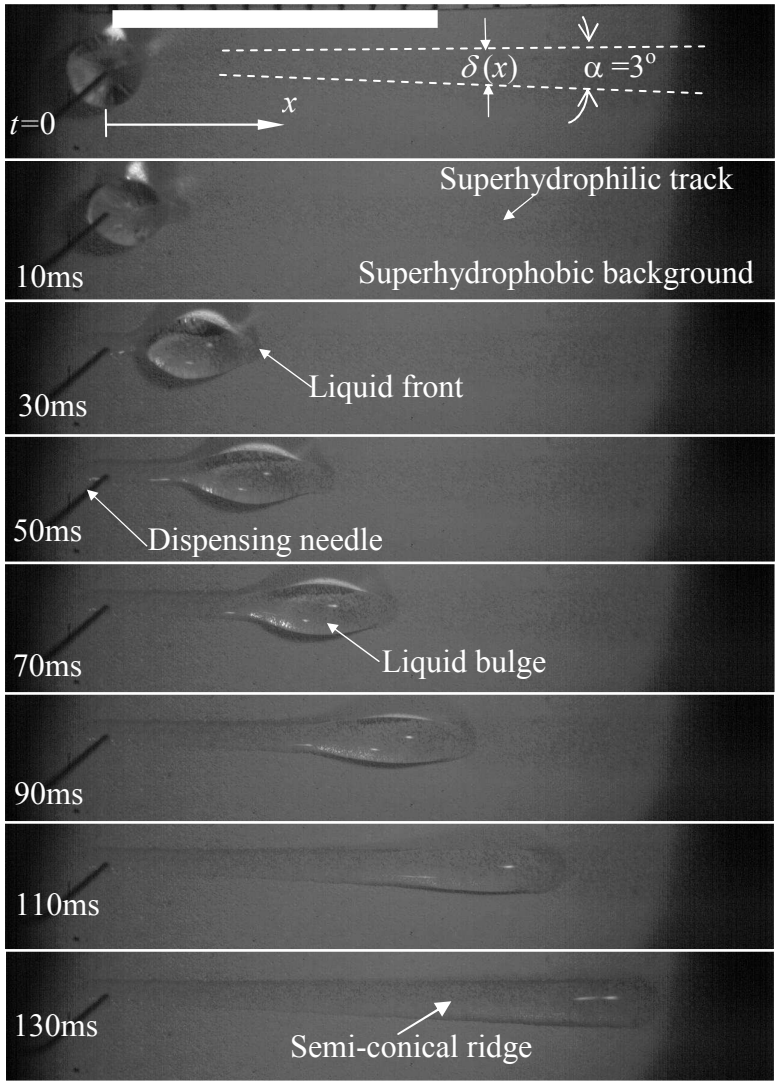

(a)

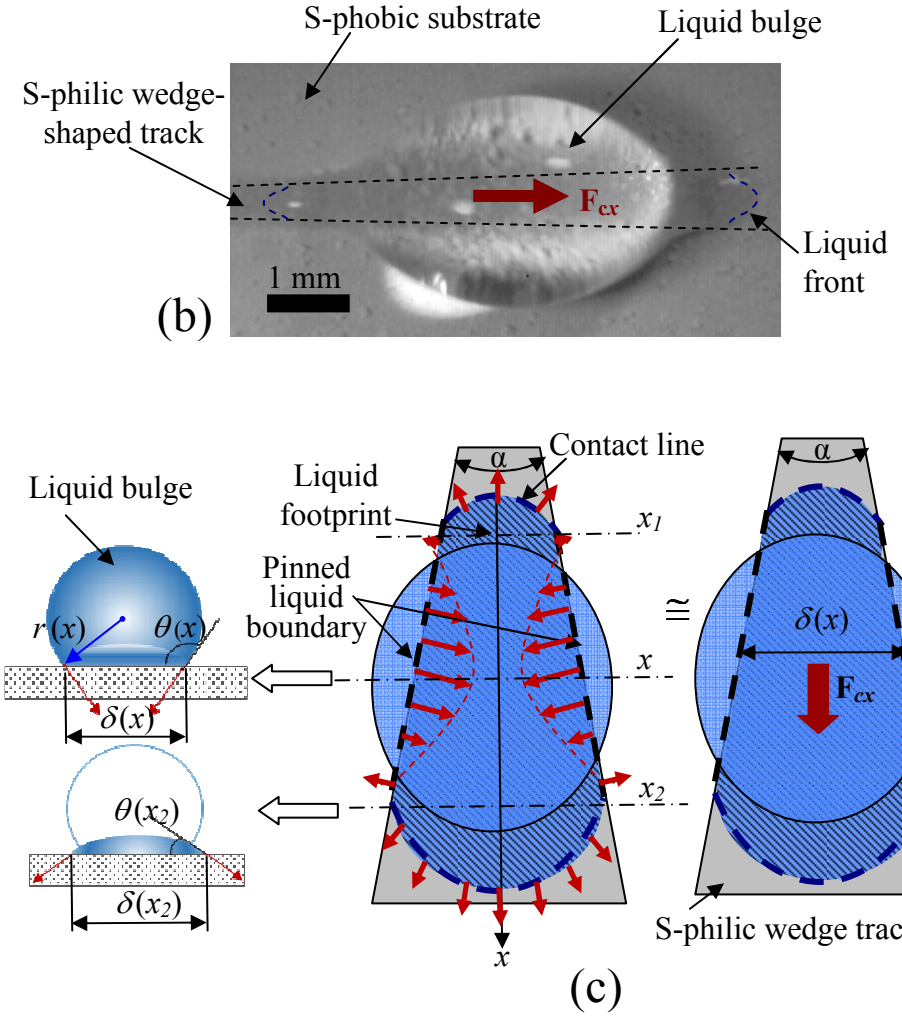

Figure 2: (a) Time-lapsed images of liquid transport through the wedge-shaped superhydrophilic track on a horizontal Al-substrate. The white bar at the top denotes 10 mm. (b) Morphology of the liquid bulge, approximated as an ellipsoid of finite footprint on the wedge-shaped superhydrophilic track, moving along the track; (c) origin of the driving capillary force on the liquid bulge.

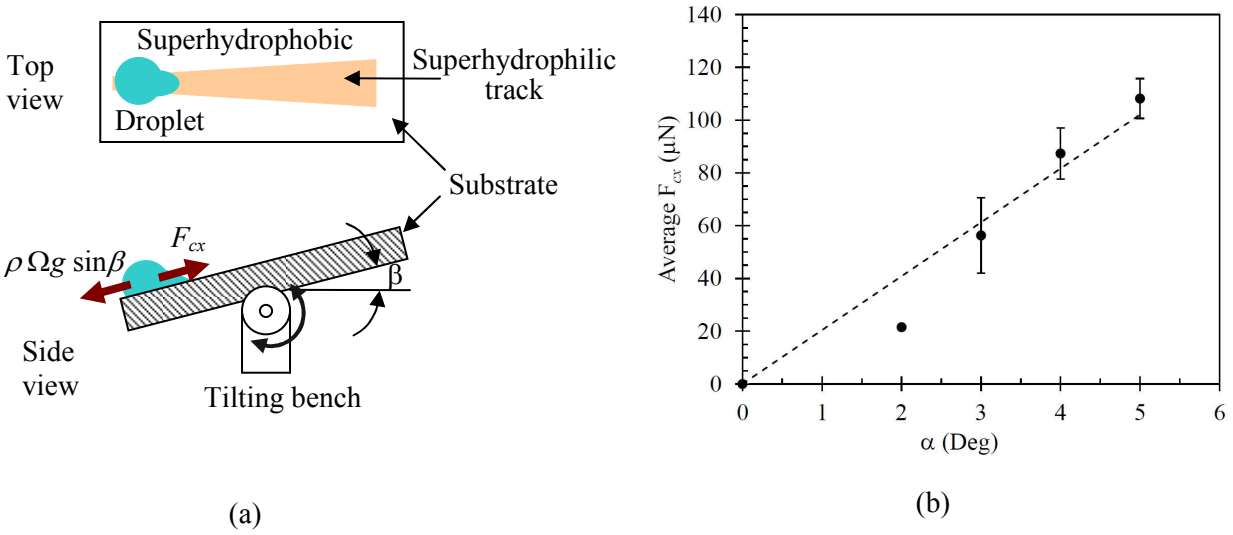

(a) (b)

Figure 3: (a) Arrangement for measurement of capillary force F_{cx} at the narrow end of the wedge at the onset of droplet motion. (b) Variation of F_{cx} with the wedge angle α (error bar shows the standard deviation in readings due to variability in droplet volume).

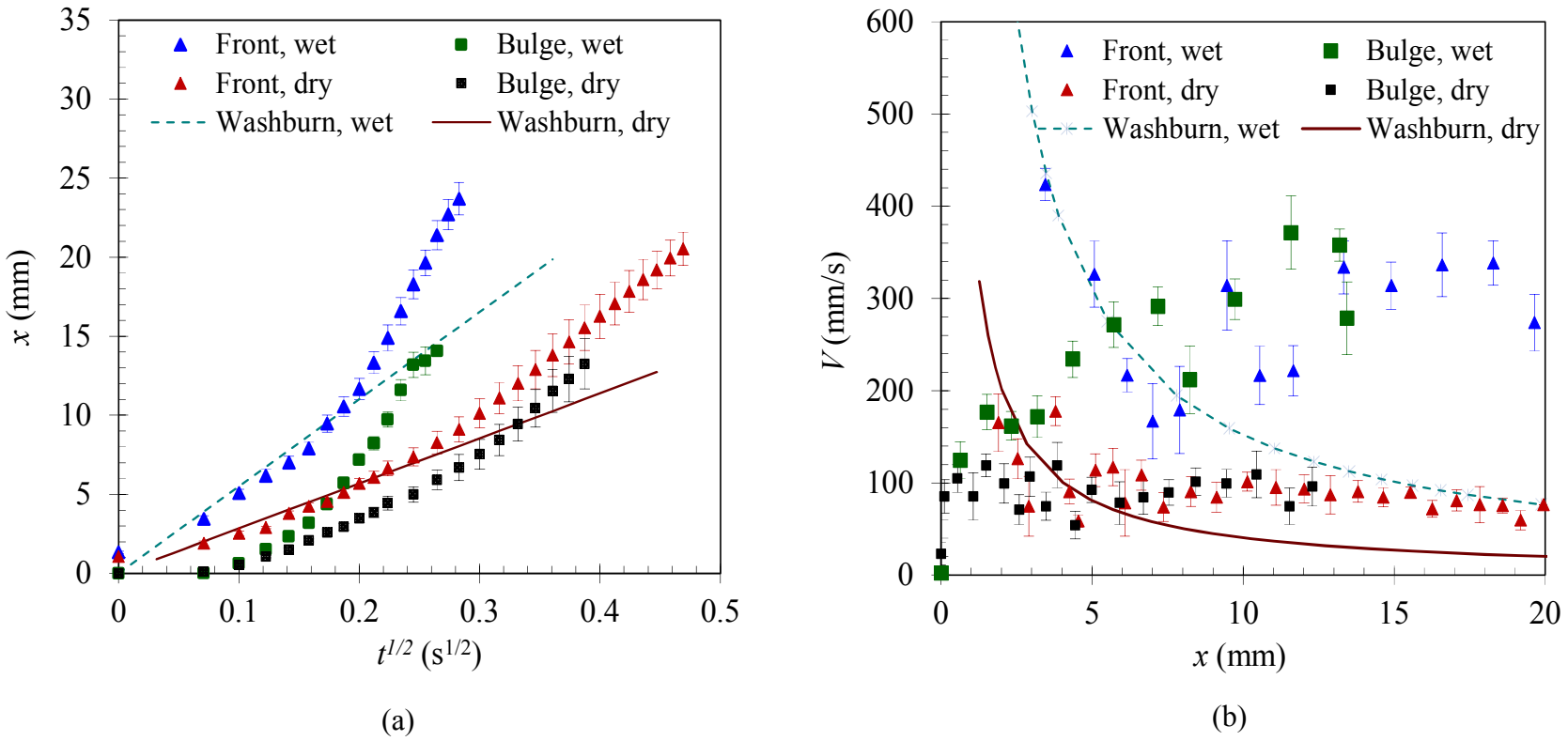

Figure 4: Transport of the liquid front and the liquid bulge along a wedge-shaped track with $\alpha = 3^{o}$ (see Fig. 2a). (a) Distance x from the dispensing location as a function of $t^{1/2}$, and (b) velocity as function of position along the track. Comparison of the experimental data (symbols) with the Washburn model for wetting behavior (continuous curves) is also made. The gray bar denotes the spatial region in which the "bulge" volume shape transformed to the spreadout rivulet shape.

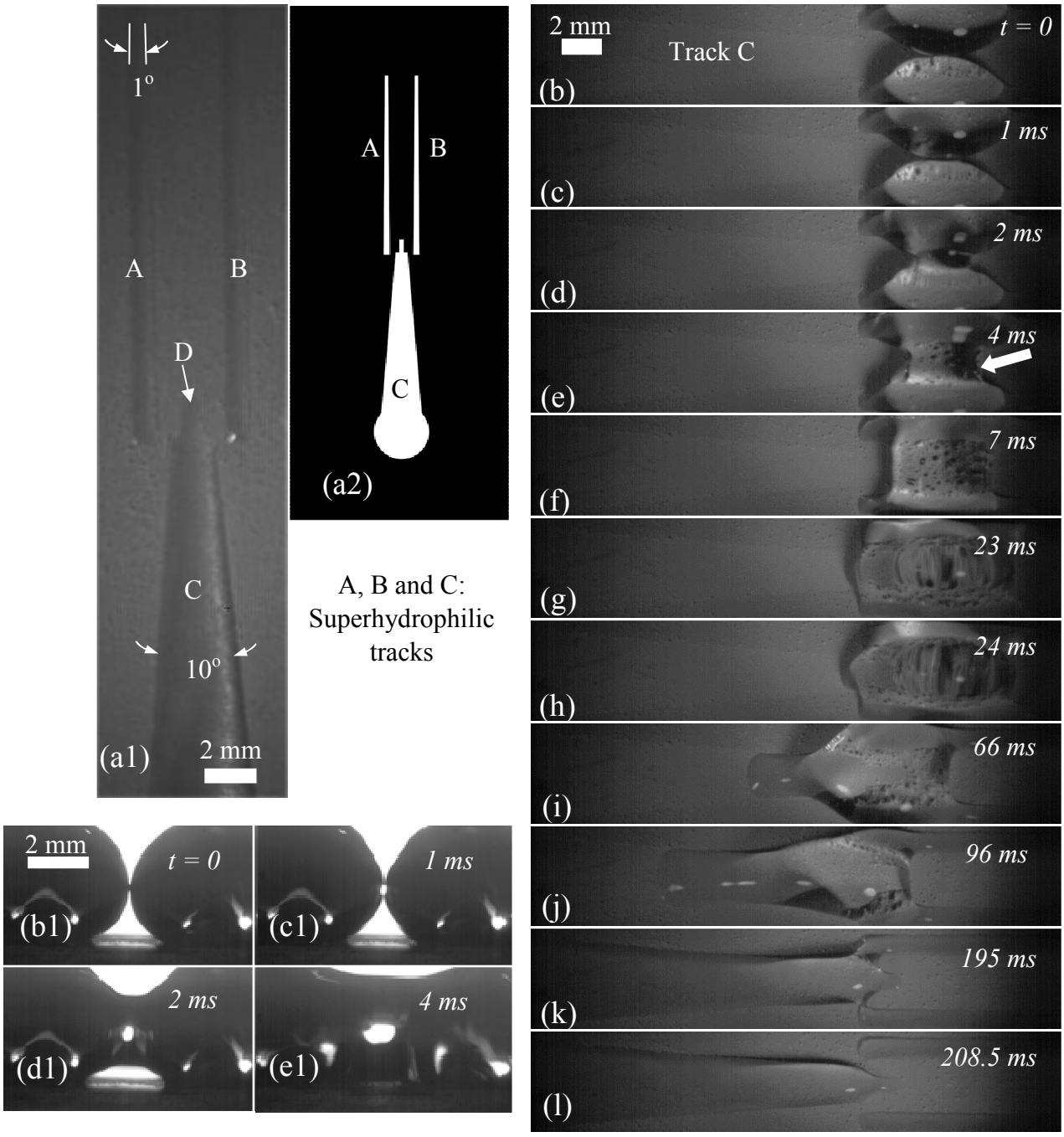

Figure 5: The patterned Al substrate (a1) and the mask (a2) used for demonstrating a multi-step functional surface device capable of performing pumpless liquid bridging and draining. Snapshots of events on the liquid bridge circuit: (b, b1) Liquid bulges at the wider ends of tracks A and B just before a liquid bridging event; (c, c1) onset of liquid bridging, (d-f) progression of liquid bridge formation; (g-h) liquid bridge touches the tongue D of track C; (i – k) progression of liquid pumping; (l) de-bridging at the end of pumping. Starting from the onset of the liquid bridge touching track D (frame (g)) to the de-bridged state (frame (l)), this procedure achieves an average pumping rate of 357 μL s^{-1}. (b1) – (e1): End views of the bridge formation and growth events (top views in (b) – (e)) as seen from the downstream delivery side of the device. Also see ESI video SM2.

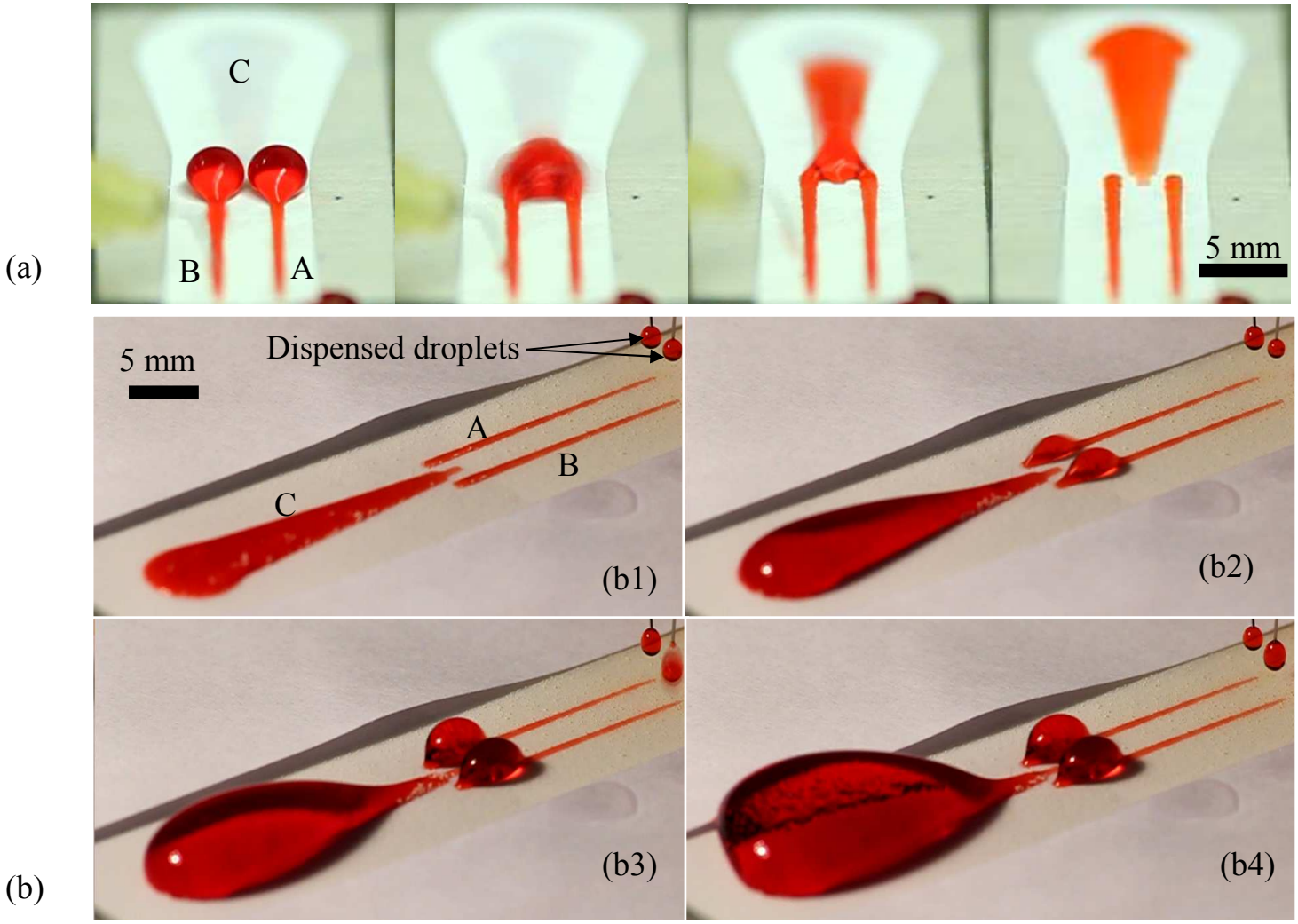

Figure 6: (a) End view sequence displaying liquid bridging and draining on the design of Fig. 5(a) applied on a horizontal paper substrate. (b) Collection of liquid on the bridge circuit on a horizontal transparency (PET) film substrate after pumping for (b1) 1 cycle (~56 µL), (b2) 4 cycles (~226 µL), (b3) 7 cycles (~395 µL), and (b4) 10 cycles (~564 µL). The liquid (water) is dyed for better visualization.

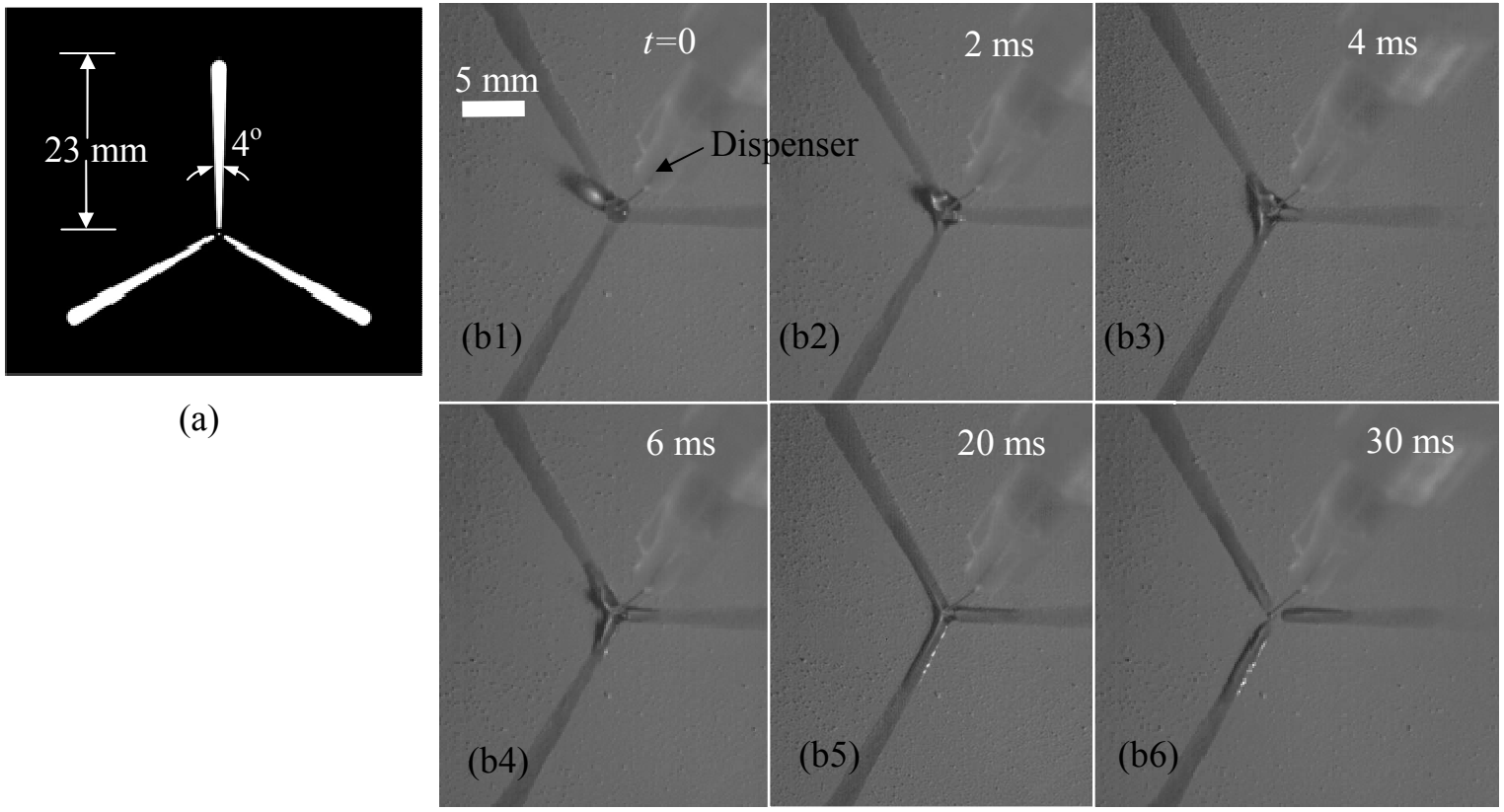

Figure 7: (a) Photomasking template for the droplet three-splitter design. (b) Time-lapsed snapshots of a complete cycle of droplet splitting on an Al substrate with 3 radially equispaced wedge tracks. The event achieves a collective average pumping rate of 157 μL s^{-1}.

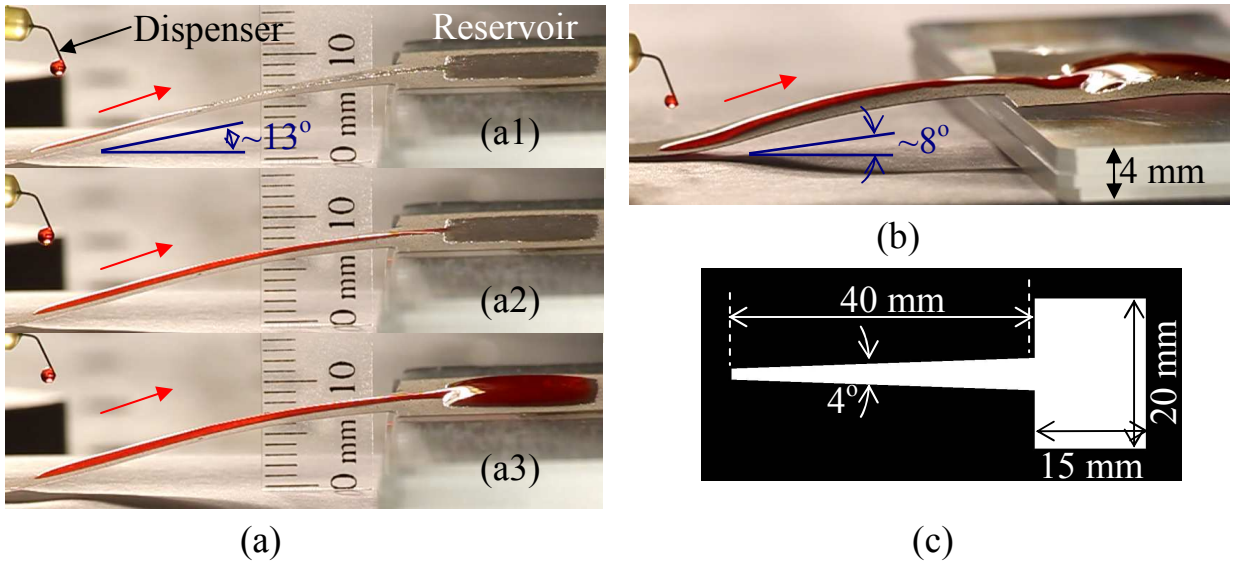

Figure 8: Transport of liquid up along an inclined superhydrophilic wedge-shaped track. (a) Snapshots of water (dyed for better visualization) being pumped up along a transparency (PET) film substrate to an elevation of 9 mm after: (a1) one drop (4.7 µL), (a2) 5 drops (23.5 µL), and (a3) 40 drops (188 µL) (see also ESI video SM4). (b) 25 droplets (117.5 µL) were pumped up a height of 4mm along an identical track on paper. (c) The photomasking template for the tracks used in (a) and (b).

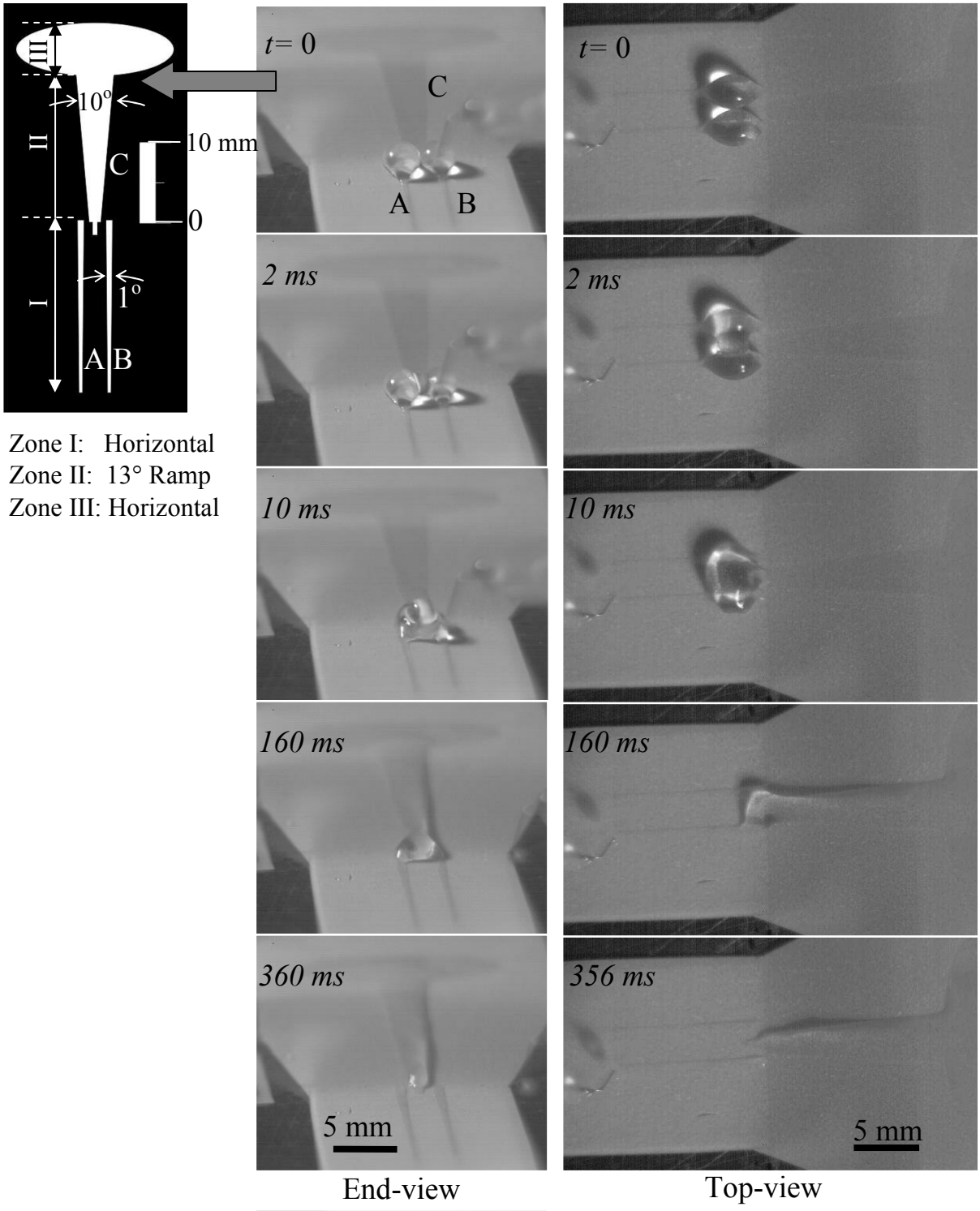

Figure 9: Snapshots of liquid transport up an inclined plane through a 13° up slope (height of ~4 mm) on a droplet bridging and draining circuit (inset at the top left corner) after dispensing 56.4 μL of liquid. End-view (left column) and top view (right column), as taken from two distinct runs under the same conditions. The needle dispenser can be seen on the left of each top-view image.